PAPER

Check for updates

Surfactant-assisted solvothermal synthesis of NiCo$_2$O$_4$ as an anode for lithium-ion batteries†

Yehua Li,[ab] Xianwen Wu, [ID] *[ab] Suliang Wang,[ab] Wenqi Wang,[ab] Yanhong Xiang,[a] Chunhui Dai,[ab] Zhixiong Liu,[a] Zeqiang He[a] and Xianming Wu[a]

Binary metal oxides have been considered as promising anode materials, which exhibit much better performances than single metal oxides in view of their variable oxidation state and fairly high electrical conductivity. In this research, NiCo$_2$O$_4$ nanocrystals are prepared from a facile procedure including microemulsion-solvothermal reaction and subsequent calcination at 400 °C for 4 hours. The as-prepared NiCo$_2$O$_4$ nanocrystals are characterized by X-ray diffraction (XRD), field-emission scanning electron microscopy (FE-SEM), transmission electron microscopy (TEM), and X-ray photoelectron spectroscopy (XPS). When applied as an anode for a lithium ion battery, it demonstrates excellent cycling and rate stability. The initial charge/discharge efficiency is as high as 75.41% at a current density of 100 mA g^{-1}. After 45 cycles, the discharge capacity still retains up to 1175.9 mA h g^{-1}, which is even much higher than that of the initial discharge capacity. Meanwhile, the reversible capacity remains over 644.9 mA h g^{-1} at a large current density of 1600 mA g^{-1}, ascribed to the dispersed nanoparticles, which will help to improve the conductivity of the electrode material during the lithium-ion insertion/deintercalation process, shorten the ion diffusion path and reduce the charge transfer resistance (R_{ct}).

Introduction

In order to develop clean, economical, efficient and safe renewable energy and its related devices for conversion and storage, lithium-ion batteries (LIBs) have been intensively investigated due to their advantages of high energy density, no environmental pollution, good cycle performance and long lifespan,[1,2] and are used in portable electronic products, electric bicycles, electric automobiles and the aerospace industry.[3] However, with the rapid development of new energy vehicles, traditional anode materials such as graphite[4] have been unable to meet the requirements for LIBs with high energy density. Compared with the traditional carbon-based electrode materials, transition metal oxides (TMOs) show great potential application due to their high energy density and high power density.[5] Among the reported TMOs, the cobalt oxide (Co$_3$O$_4$) has exhibited the promising electrochemical performances as an anode material for LIBs owing to its advantages of abundant resources, low production cost and high capacity with 890 mA h g^{-1}.[6]

However, cobalt resource is expensive and toxic, which seriously limits its practical application. Thus, Co is partially substituted by the use of inexpensive and non-toxic metal elements[7] and various binary TMOs are investigated including FeCo$_2$O$_4$,[8] ZnCo$_2$O$_4$,[9] NiCo$_2$O$_4$.[10–13] Compared with Co$_3$O$_4$, the spinel structure NiCo$_2$O$_4$ is similar to that of Co$_3$O$_4$. Besides, Ni/Ni and Co/Co solid-phase redox reaction pairs also exist in NiCo$_2$O$_4$, which makes it display excellent electrochemical performances.[14] To date, it has been received great attention from researchers. However, there is low initial coulombic efficiency for NiCo$_2$O$_4$.[15,16] Moreover, the volume expansion of NiCo$_2$O$_4$ causes the electrode to be powdered during the charge/discharge process, so that the contact between NiCo$_2$O$_4$ particles and the current collector becomes worse, leading to the rapid decay of the specific capacity of NiCo$_2$O$_4$ particles. Meanwhile, the slow diffusion rates of electron and lithium-ion result in the poor rate performance,[17] all of which above hinder its application as anode material of LIBs.

In order to solve these problems, many synthesis approaches about NiCo$_2$O$_4$ have been developed including coprecipitation,[18] hydrothermal/solvothermal,[19,20] spray pyrolysis,[21] electrospinning[22] and so on. However, the reported reversible capacity for NiCo$_2$O$_4$ hollow spheres and nanosheets and so on is not up to 600 mA h g^{-1} at large current density of 1000 mA g^{-1}.[21,23,24] Different from the above synthetic methods, microemulsion approach equips with large interfacial area and ultra-low interfacial tension. Solvothermal synthesis of nanomaterials can not only reduce the reaction temperatures, but also improve the crystallinity of the products. In order to ensure the good crystallinity and dispersion of nanomaterials,

[a]*The Collaborative Innovation Center of Manganese-Zinc-Vanadium Industrial Technology, Jishou University, Jishou 416000, P. R. China. E-mail: wxwcsu2011@163.com*

[b]*School of Chemistry and Chemical Engineering, Jishou University, Jishou 416000, P. R. China*

microemulsion-solvothermal approach has become one of the effective methods to prepare inorganic nanocrystals with uniform morphology.[25]

Herein, in this work, we reported a facile surfactant-assisted solvothermal method to prepare the $NiCo_2O_4$ anode material for LIBs at about 100 °C and the electrochemical performance were investigated carefully at the same time.

Experimental

The schematic illustration of the formation of $NiCo_2O_4$ nanocrystals is indicated in Fig. 1. All the chemicals with analytical grade were purchased from Sinopharm Chemical Reagent Co., Ltd and used without further purification. A typical experimental procedure was used as follows. 1.5 g cetyltrimethylammonium bromide (CTAB) was dissolved into deionized water (2 ml), n-pentanol ($C_5H_{12}O$, 3 ml) and cyclohexane (C_6H_{12}, 60 ml) under the magnetic stirring for 1 hour. Then 5 mmol of cobalt nitrate hexahydrate ($Co(NO_3)_2 \cdot 6H_2O$) and 2.5 mmol of nickel nitrate hexahydrate ($Ni(NO_3)_2 \cdot 6H_2O$) were added to the solution, followed by the precipitation of 30 mmol urea ($CO(NH_2)_2$). After being magnetic stirred for 1.5 hour, the solution was then transferred to a Teflon-lined stainless steel autoclave and was maintained at 100 °C for 10 hour. When it was naturally cooled to room temperature, the precursor was washed with distilled water and anhydrous alcohol for several times, collected by centrifuge. Then it was dried at 60 °C for 12 hour so as to obtain the precursor of $NiCo_2O_4$. Finally, $NiCo_2O_4$ products were obtained after heated at 400 °C for 4 hours.

X-ray diffraction (XRD, D8 Discover, Bruker) was employed to determine the phase and structure of as-prepared products with Cu Kα radiation ($\lambda = 0.1518$ nm) from 5° to 80°. The field-emission scanning microscopy (FE-SEM, Leo-1530, Zeiss) with an accelerating voltage of 20 kV and transmission electron microscopy (TEM, Tecnai G12, 200 kV) were used to investigate the morphology and microstructure. Thermogravimetric analysis (TGA, SDT Q600, TA instruments) for the precursor of $NiCo_2O_4$ was performed in air from 20 °C to 800 °C with a heating rate of 10 °C min^{-1}. The surface element analysis of the as-synthesized product was used by X-ray photoelectron spectroscopy (XPS, K-Alpha 1063), and then the spectra obtained was fitted using XPS peak software (version 4.1).

The working electrode was prepared by casting slurries of 80 wt% $NiCo_2O_4$, 10 wt% acetylene black and 10 wt%

polyvinylidene fluoride (PVDF) in N-methyl-2-pyrrolidinone (NMP) on Cu foil current collector. Then it was placed in an oven at 120 °C for 6 hour for drying. After being cooled to room temperature, the electrode was punched into a circular electrode with a diameter of 14 mm. Next, the electrode sheet was placed in a vacuum oven and dried at 60 °C for 12 hour. Lastly, the batteries were assembled in a glove box filled with high-purity argon. Celgard 2300 porous polypropylene film was used as the separator, and the electrolyte was 1 mol L^{-1} LiPF$_6$ (EC, DEC and DMC were mixed in a volume ratio of 1 : 1 : 1). The galvanostatic charge–discharge tests of the batteries were used with the Neware BTS-5V/5 mA between 0.01 V and 3.0 V. The cyclic voltammetry (CV) between 0.01 V and 3 V at a scanning rate of 0.1 mV s^{-1} and electrochemical impedance spectroscopy (EIS) of the batteries at discharged state were measured by using CHI660E electrochemical workstation (Shanghai Chenhua), the EIS was performed with the perturbation amplitude of 5 mV in the frequency range of 10^{-2} Hz to 10^5 Hz.

Results and discussion

In the microemulsion system, the size of the droplets can be altered by varying the W value ($W = H_2O$/surfactant, molar ratio). Thus, the formation of nanoparticles size can be further controlled.[26] When the W value is between 10 and 20, the nanoparticles with the size of 15–30 nm can be obtained. In this work, reverse micelles made of CTAB–n-pentanol–cyclohexane–water were used in preparation of the $NiCo_2O_4$ nanocrystals with W value at 13.5. The possible formation process of $NiCo_2O_4$ nanocrystals are shown in Fig. 1. Firstly, the electrostatic repulsions between CTA$^+$ and Co^{2+}, Ni^{2+} made better dispersion of the sample particles, and the nickel–cobalt hydroxycarbonate precursor was formed by the reaction of metal ions with anions (CO_3^{2-} and OH$^-$), which was produced through the slow hydrolysis of urea. Subsequently, $NiCo_2O_4$ nanocrystals were obtained by annealing the Ni–Co precursor in air. According to the previous report, solvent heat and annealing reactions occurred during the synthesis process, which can be described as follows from eqn (1) to (5).[27]
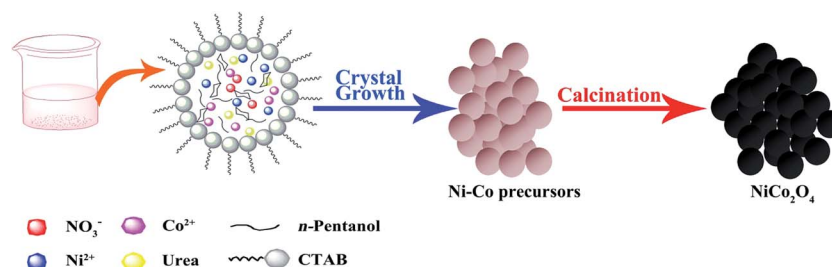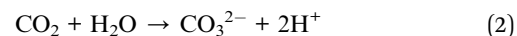
$$CO(NH_2)_2 + H_2O \rightarrow 2NH_3 + CO_2 \tag{1}$$

$$CO_2 + H_2O \rightarrow CO_3^{2-} + 2H^+ \tag{2}$$

Fig. 1 Schematic illustration of the formation of $NiCo_2O_4$ nanocrystals through microemulsion-solvothermal growth and subsequent calcination in air.

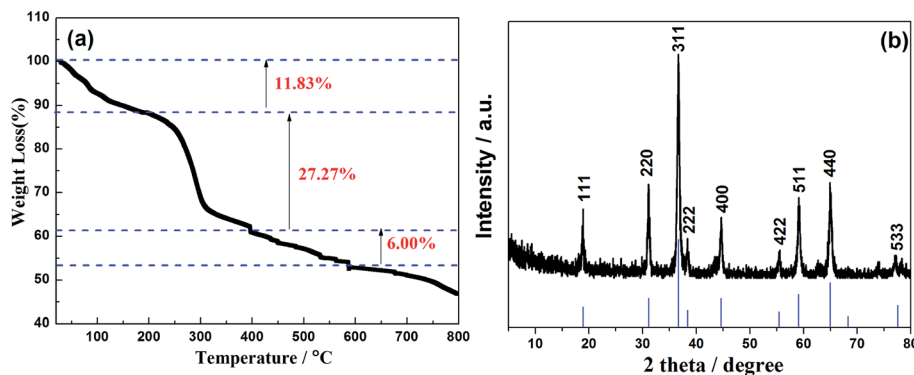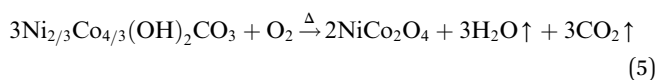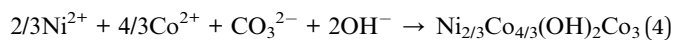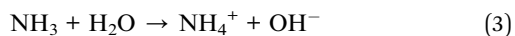Fig. 2   (a) The TGA curves of precursor and (b) XRD pattern of $NiCo_2O_4$.

$$NH_3 + H_2O \rightarrow NH_4^+ + OH^- \tag{3}$$

$$2/3Ni^{2+} + 4/3Co^{2+} + CO_3^{2-} + 2OH^- \rightarrow Ni_{2/3}Co_{4/3}(OH)_2Co_3 \tag{4}$$

$$3Ni_{2/3}Co_{4/3}(OH)_2CO_3 + O_2 \xrightarrow{\Delta} 2NiCo_2O_4 + 3H_2O\uparrow + 3CO_2\uparrow \tag{5}$$

In order to confirm the annealing temperature of the as-obtained samples, the thermogravimetric analysis (TGA) was investigated in Fig. 2a. It is obvious that the first weight losses of the precursors from 20 °C to 200 °C are attributed to the water evaporation physically adsorbed and the loss of the thermal decomposition of crystal water in the hydroxyl carbonate precursors. The second 27.27% weight loss at 200–400 °C owes to the conversion of anhydrous precursors to spinel cubic crystals of $NiCo_2O_4$. In addition, the weight of loss between 400–550 °C is attributed to the removal of residual carbon. Meanwhile, the weight loss over 550 °C is mainly due to decomposition of $NiCo_2O_4$, which is confirmed from the XRD of $NiCo_2O_4$ by calcining the precursors at 600 °C in Fig. SI-1.† Therefore,

based on the TGA curves and XRD result, the calcination temperature of as-synthesized $NiCo_2O_4$ at 400 °C is not only to ensure the complete conversion of the precursors,[28–30] but also to avoid the oxidation of carbon and the decomposition of $NiCo_2O_4$, which will increase the rate performance of the battery to a certain extent.

The XRD was used to examine the crystal structure and phase purity of the prepared products. As shown in Fig. 2b, the powder XRD pattern of $NiCo_2O_4$ has good crystallinity with high peak intensity. The 2θ values of 18.9, 31.1, 36.7, 38.4, 44.6, 55.4, 59.1 and 65.0 correspond to the typical diffraction peaks at (111), (220), (311), (222), (400), (422), (511) and (440) crystal planes, respectively, which are consistent with the cubic spinel $NiCo_2O_4$ phase (JCPDS no. 20-0781). There is no distinct impurity peaks to be detected, indicating that the Ni–Co precursors have fully oxidized to pure $NiCo_2O_4$ after calcination at 400 °C. The average lattice constant is 0.81245 nm, and the cell volume is 0.5363 nm^3, which is a little higher than that of 0.5342 nm^3 for the PDF card of $NiCo_2O_4$. Further, the particle size of (311) crystal plane according to the Scherrer equation is calculated to
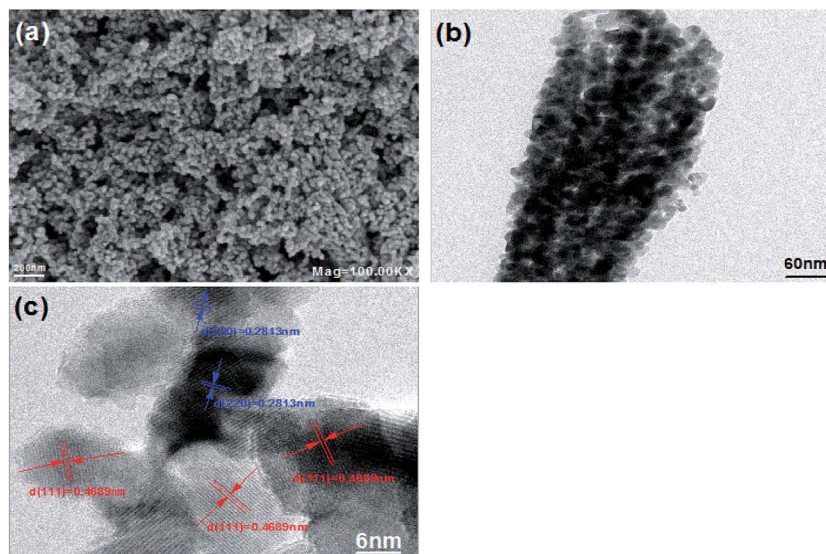

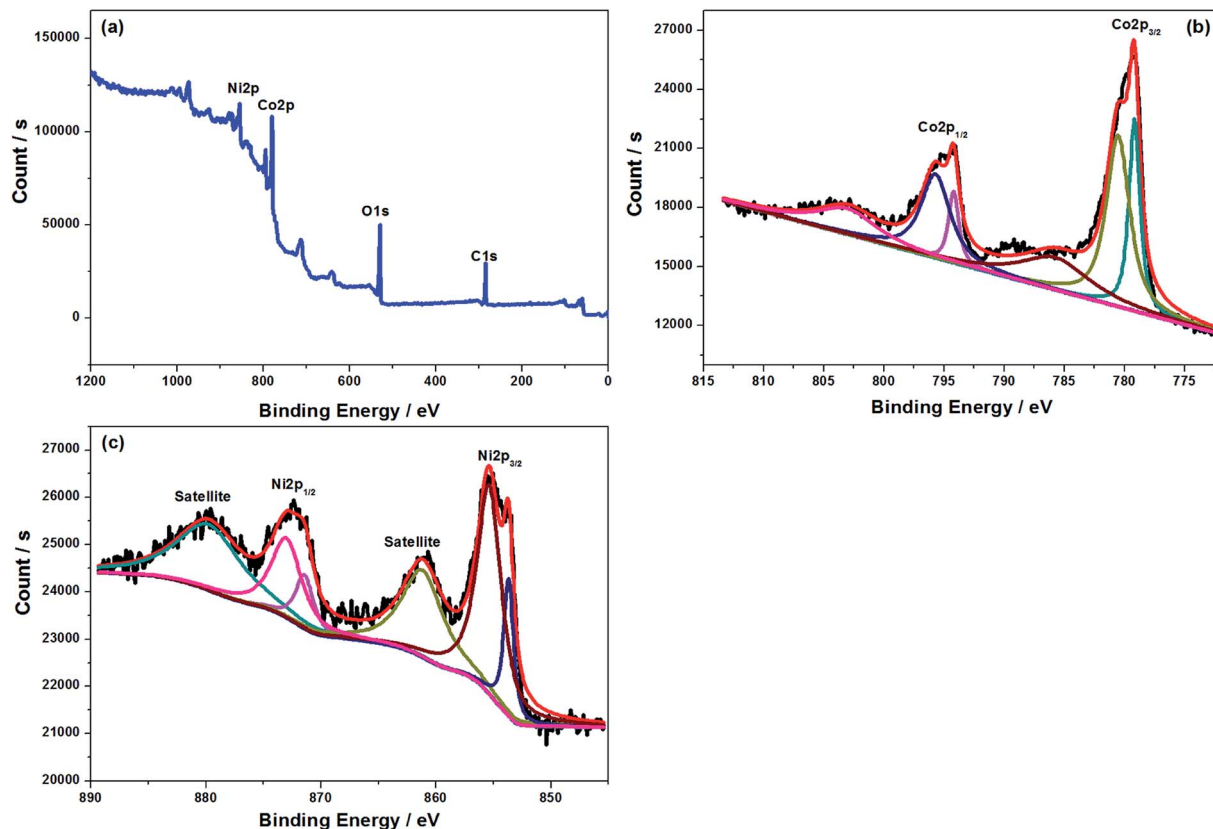Fig. 3   (a) The SEM, (b) TEM and (c) HRTEM of $NiCo_2O_4$.

Fig. 4 XPS spectra of $NiCo_2O_4$ (a) survey spectrum; (b) Co 2p spectrum and (c) Ni 2p spectrum.

be 29.14 nm and the average particle size of material is 24.9 nm, indicating the existence of the extremely fine nanoparticles. Thus, it will further shorten the diffusion path of lithium ions and increase the reaction sites and electrolyte contact areas and help to improve the electrochemical performances of the active materials.

SEM and TEM are usually used to evaluate the morphology and microstructure of the as-prepared $NiCo_2O_4$, as shown in Fig. 3. Obviously, a number of dispersive spherical nanocrystals are formed from SEM in Fig. 3a and TEM in Fig. 3b, facilitating the electronic transmission and improving the rate performance of the battery. In order to further investigate the microstructure of the sample, the high-resolution transmission electron microscopy (HRTEM) image in Fig. 3c displays that the lattice space of 0.2813 nm and 0.4689 nm correspond to the (220) and (111) crystal planes of the spinel $NiCo_2O_4$ phase, respectively.

To further explore the element component and oxygen state of the powders, X-ray photoelectron spectroscopy (XPS) was performed, and the corresponding results are presented in Fig. 4 and SI-2.† The full scanning spectrum of $NiCo_2O_4$ indicates the presence of Ni, Co and O as well as C elements. It can be noted that the signal of C 1s located at 284.9 eV and 288.8 eV can be detectable. For one thing, it is used as the reference for calibration. For another, there are some residual carbons in the sample, which is consistent with the TGA analysis, facilitating the C-rate improvement of the battery. The high resolution

spectrum of Ni 2p has a pair of spin–orbit peaks (Ni $2p_{1/2}$ and Ni $2p_{3/2}$) and double satellite peaks. Correspondingly, two typical peaks of nickel are detected, belonging to Ni^{2+} and Ni^{3+}, respectively. In addition, the Co 2p spectrum can be fitted to a pair of spin–orbit peaks (Co $2p_{1/2}$ and Co $2p_{3/2}$) and two satellite peaks which are assigned to the characteristic of Co^{2+} and Co^{3+}. The high-resolution O 1s peak can be separated into three sub-peaks. The fitting peak at 528.9 eV represents a typical metal–oxygen bond, and the fitting peak with a binding energy of 531.2 eV is attributed to the oxygen in the OH group. It exhibits that the surface of $NiCo_2O_4$ is hydroxylated, which may be caused by the hydroxide component remaining on the surface of the materials. The fitting peak at 532.4 eV corresponds to a large number of defects in the hypoxia coordination, which is usually observed in nanoparticle materials, making it easy for the lithium ion diffusion.

Fig. 5a shows cyclic voltammetry profiles at the initial three cycles in the range of 0.01–3 V *versus* Li/Li$^+$ at a sweeping rate of 0.1 mV s^{-1}. Notably, the first cycle is obviously different from the subsequent ones. During the initial cathodic scanning process, the first reduction peak located at about 1.31 V can be attributed to destruction and/or amorphization of their crystal structure.[31] The second obvious reduction peak at 0.93 V corresponds to the reduction of Ni^{2+} and Co^{3+} into their metallic Ni^0 and Co^0 and the formation of amorphous Li_2O. Another smaller reduction peak at 0.61 V may be assigned to the irreversible decomposition of the electrolyte, resulting in the
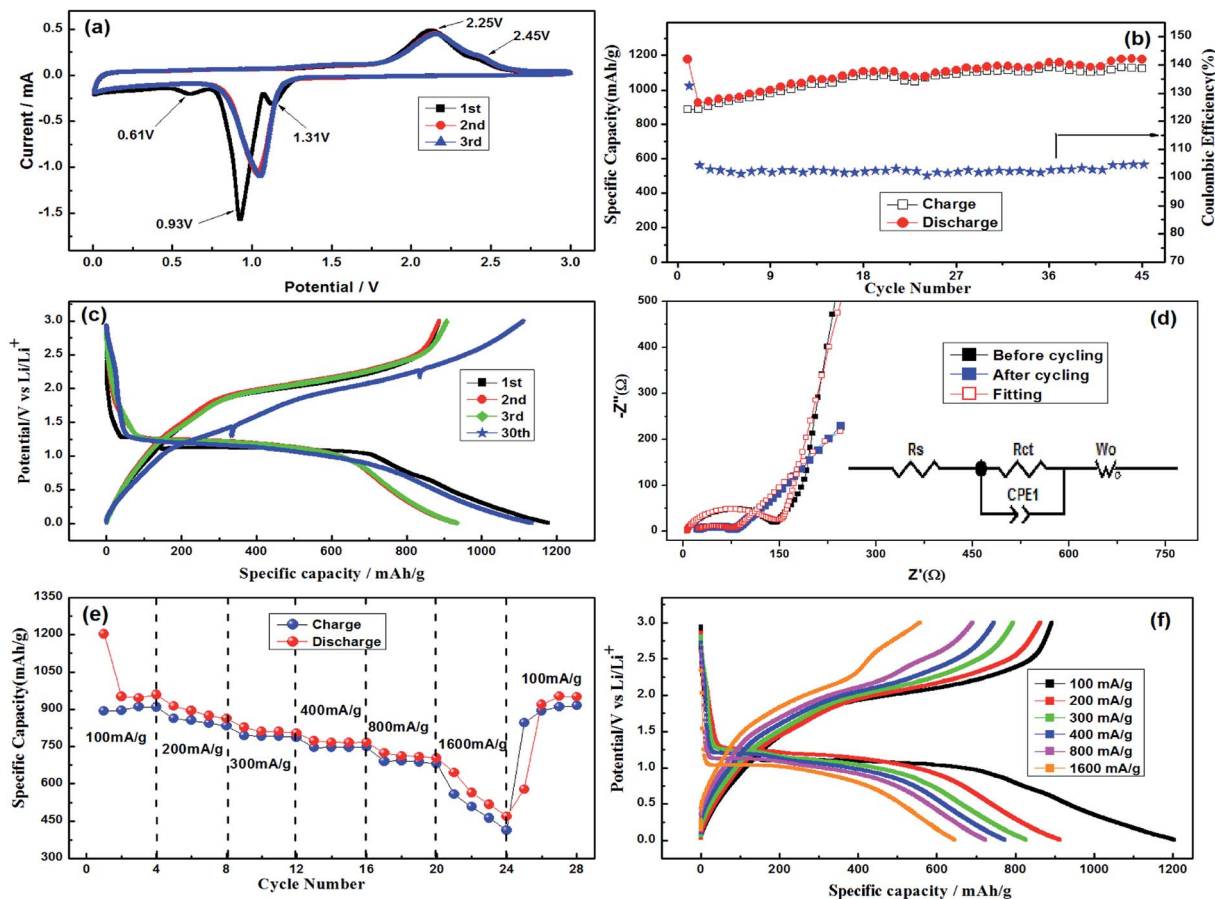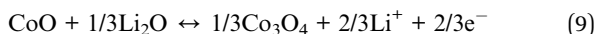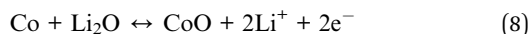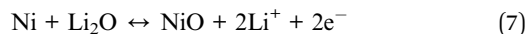
Fig. 5 (a) The cyclic voltammetry curves of $NiCo_2O_4$/Li at a scan rate of 0.1 mV s^{-1}, (b and c) the cycling performance, (d) EIS spectra and the fitting curves of the battery before and after cycling, (e and f) rate performance.

formation of the solid electrolyte interface (SEI). During the reverse anodic scanning process, two oxidation peaks at the potentials of 2.25 V and 2.45 V are observed, corresponding to the oxidation of Ni^0 and Co^0, respectively, which are consistent with the voltage plateaus in the charge curve. The position and area of the cathodic and anodic peaks are overlapped after the second cycle, which means that the electrochemical reaction of the active materials tends to be stable, resulting in good cycling stability and electrochemical reversibility. The above specific reactions are shown in eqn (6)–(9).[31,32]

$$NiCo_2O_4 + 8Li^+ + 8e^- \rightarrow Ni + 2Co + 4Li_2O \quad (6)$$

$$Ni + Li_2O \leftrightarrow NiO + 2Li^+ + 2e^- \quad (7)$$

$$Co + Li_2O \leftrightarrow CoO + 2Li^+ + 2e^- \quad (8)$$

$$CoO + 1/3Li_2O \leftrightarrow 1/3Co_3O_4 + 2/3Li^+ + 2/3e^- \quad (9)$$

As shown in Fig. 5b and c, the constant current charge/discharge curves of the as-prepared $NiCo_2O_4$ electrode was measured at a current density of 100 mA g^{-1} in the range of 0.01–3 V. The initial discharge capacity and the initial coulombic efficiency of the battery are up to 1176.5 mA h g^{-1} and 75.41%,

respectively. However, the coulombic efficiency of the battery increased rapidly to 93.50% after the first cycle. As the cycle number increases, the insertion–exertion lithium capacity of the electrode gradually tends to increase and then to be stable. Even after 45 cycles, the discharge and charge capacity are up to 1175.9 mA h g^{-1} and 1123.6 mA h g^{-1}, respectively, which are much higher than those of the first cycle and the reported values in Table SI-1.† The increase of the reversible capacity may be due to the increasing number of electrochemical reaction sites.[31] Herein, the morphology of $NiCo_2O_4$ electrode after 45 cycles was tested in Fig. SI-3.† It can be seen that $NiCo_2O_4$ remains its perfect nanoparticles, which does not fall off from the copper current collector, indicating the excellent cyclic stability.

The electrochemical impedance behavior of the $NiCo_2O_4$ electrode before and after cycling tests at 100 mA g^{-1} was investigated by electrochemical impedance spectroscopy (EIS), as

Table 1 Impedance parameters of equivalent circuit of $NiCo_2O_4$/Li

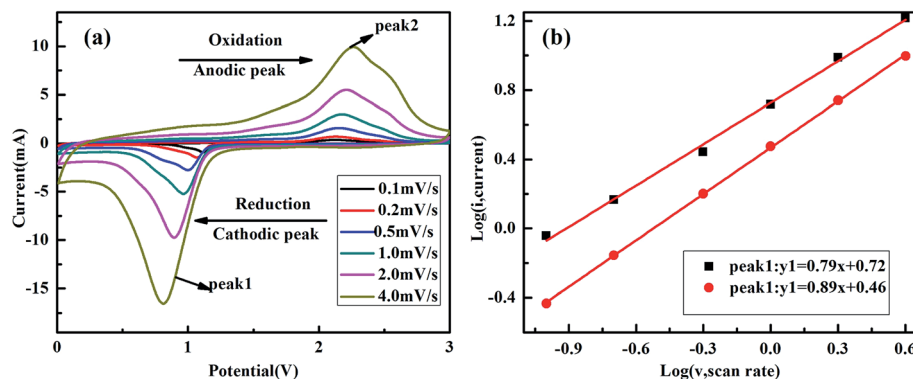| Sample	Fresh		45th cycles	
	R_s (Ω)	R_{ct} (Ω)	R_s (Ω)	R_{ct} (Ω)
$NiCo_2O_4$	5.151	132.3	12.55	72.87

Fig. 6 (a) The cyclic voltammograms of $NiCo_2O_4$ at various scan rates from 0.1 to 4.0 mV s^{-1} and (b) the functional relationship between the peak current density (i) and scan rate (v) in logarithmic algorithm.

shown in Fig. 5d. The curve consists of two parts, a semicircle at high frequency and sloping line at low frequency. The semicircle corresponds to the charge transfer resistance (R_{ct}) and double layer capacitance (C_{dl}). The sloping line represents the Warburg impedance (Z_ω), which is related to the diffusion coefficient of Li$^+$ in the solid phase. The kinetic parameters of the $NiCo_2O_4$ electrodes are listed in Table 1. The smaller R_{ct} of the battery with 132.3 Ω means the fast charge transfer rate of the electrode. However, the R_{ct} decreased to 72.87 Ω even after 45th cycles, which may be attributed to the activated electrode materials.

In order to further confirm the advantages of the sample for lithium storage, the rate performance of the sample was also evaluated, as shown in Fig. 5(e) and (f). It delivered the discharge capacities of 1203.2, 894.1, 810.2, 772.6, 723.4 mA h g^{-1} at different current densities of 100, 200, 300, 400 and 800 mA g^{-1}, respectively. As the current density is increased to 1600 mA g^{-1}, the capacity is still maintained over 644.9 mA h g^{-1}. While the current density was returned from 1600 mA g^{-1} back to 100 mA g^{-1} after 24 cycles, the reversible capacity of the electrode can also be restored to 950.7 mA h g^{-1}. The results indicate that even though the electrode was circulated at a large current density, the structure of the materials was still unbroken and maintained perfect contact with the current collector. The excellent rate performance is due to the dispersive nanoparticles of $NiCo_2O_4$, which will help to shorten the diffusion path of lithium ions and alleviate the volume expansion during intercalation/deintercalation process, increasing the conductivity of the electrode.

To further investigate the excellent rate performance, the CVs of as-prepared $NiCo_2O_4$ electrode at different scan rates between 0.1 mV s^{-1} and 4.0 mV s^{-1} are measured in Fig. 6. Apparently, the peak current is not proportional to the square root of the sweep speed with the scan rate increasing, indicating that the lithiation/delithiation process consist of faradaic and non-faradaic behavior, which could be confirmed based on the following equation to clarify the relationship between scan rate (v) and peak current (i).[33,34]

$$i = kv^e \tag{10}$$

$$\log(i) = \log(k) + e \log(v) \tag{11}$$

where k and e are variable parameters and the e value can be defined as the way of Li-ion insertion/extraction. As the parameter of e value is 1/2, the electrochemical reaction is completely controlled by non-faradaic behavior (ionic diffusion). While the e value is 1.0, it is mainly dominated by faradaic behavior (pseudo-capacitive). The linear fitting correlation between $\log(v)$ and $\log(i)$ plots for every peak potential is depicted in Fig. 6b. The values of e for the two peaks are 0.79 and 0.89, respectively, which further illustrate that the electrochemical reactions of the $NiCo_2O_4$ electrodes are mainly determined by the faradaic behavior, resulting in rapid lithium-ion diffusion behavior.

Conclusions

In summary, the one-dimensional $NiCo_2O_4$ were constructed through microemulsion-solvothermal approach at low reaction temperature, the growth process and the growth mechanism were explored correspondingly. As they were used as anode materials for lithium ion batteries, it displayed the higher initial charge/discharge efficiency of 75.41% at a current density of 100 mA g^{-1}. Even after 45 cycles, the discharge capacity of the battery was up to 1175.9 mA g^{-1}. It indicated excellent electrochemical performances, which was attributed to the alleviated volume expansion of electrode material during the lithium-ion insertion/deintercalation process, the shortened ion diffusion path and the smaller charge transfer resistance (R_{ct}). We believe that the preparation of spherical nano $NiCo_2O_4$ may be extended to other transition metal oxide materials for lithium ion batteries in the future.

Acknowledgements

Student of Hunan Province (JDY16015), which were greatly appreciated.

References

1 P. Poizot, S. Laruelle, S. Grugeon, *et al.*, Nano-sized transition-metal oxides as negative-electrode materials for lithium-ion batteries, *Nature*, 2000, **407**, 496–499.

2 J. C. Zheng, Y. D. Han, D. Sun, *et al.*, In situ-formed $LiVOPO_4@V_2O_5$ core-shell nanospheres as a cathode material for lithium-ion cells, *Energy Storage Materials*, 2017, **7**, 48–55.

3 J. X. Wang, Z. M. Liu, G. C. Yan, *et al.*, Improving the electrochemical performance of lithium vanadium fluorophosphate cathode material: focus on interfacial stability, *J. Power Sources*, 2016, **329**, 553–557.

4 Y. P. Wu, C. Jiang, C. Wan, *et al.*, Modified natural graphite as anode material for lithium ion batteries, *J. Power Sources*, 2002, **111**(2), 329–334.

5 L. W. Ji, Z. Lin, M. Alcoutlabi, *et al.*, Recent developments in nanostructured anode materials for rechargeable lithium-ion batteries, *Energy Environ. Sci.*, 2011, **4**(8), 2682–2699.

6 J. N. Tiwari, R. N. Tiwari and K. S. Kim, Zero-dimensional, one-dimensional, two-dimensional and three-dimensional nanostructured materials for advanced electrochemical energy devices, *Prog. Mater. Sci.*, 2012, **57**(4), 724–803.

7 X. Wang, W. S. Liu, X. H. Lu, *et al.*, Dodecyl sulfate-induced fast faradic process in nickel cobalt oxide-reduced graphite oxide composite material and its application for asymmetric supercapacitor device, *J. Mater. Chem.*, 2012, **22**(43), 23114–23119.

8 H. F. Zhu, Y. F. Sun, X. Zhang, *et al.*, Evaporation-induced self-assembly synthesis of mesoporous $FeCo_2O_4$ octahedra with large and fast lithium storage properties, *Mater. Lett.*, 2016, **166**, 1–4.

9 L. Y. Guo, Q. Ru, X. Song, *et al.*, Mesoporous $ZnCo_2O_4$ microspheres as an anode material for high-performance secondary lithium ion batteries, *RSC Adv.*, 2015, **5**(25), 19241–19247.

10 J. F. Li, S. L. Xiong, Y. R. Liu, *et al.*, High electrochemical performance of monodisperse $NiCo_2O_4$ mesoporous microspheres as an anode material for Li-ion batteries, *ACS Appl. Mater. Interfaces*, 2013, **5**(3), 981–988.

11 J. Pu, Z. Q. Liu, Z. H. Ma, *et al.*, Structure design of $NiCo_2O_4$ electrodes for high performance pseudocapacitors and lithium-ion batteries, *J. Mater. Chem. A*, 2016, **4**(44), 17394–17402.

12 T. Li, X. H. Li, Z. X. Wang, *et al.*, A novel $NiCo_2O_4$ anode morphology for lithium-ion batteries, *J. Mater. Chem. A*, 2015, **3**, 11970–11975.

13 Y. Q. Zhu and C. B. Cao, A simple synthesis of two-dimensional ultrathin nickel cobaltite nanosheets for electrochemical lithium storage, *Electrochim. Acta*, 2015, **176**, 141–148.

14 A. K. Mondal, D. W. Su, S. Q. Chen, X. Q. Xie and G. X. Wang, Highly porous $NiCo_2O_4$ nanoflakes and nanobelts as anode materials for lithium-ion batteries with excellent rate capability, *ACS Appl. Mater. Interfaces*, 2014, **6**(17), 14827–14835.

15 R. Alcántara, M. Jaraba, P. Lavela, *et al.*, $NiCo_2O_4$ spinel: first report on a transition metal oxide for the negative electrode of sodium-ion batteries, *Chem. Mater.*, 2002, **14**(7), 2847–2848.

16 A. Thissen, D. Ensling, F. J. Fernández Madrigal, *et al.*, Photoelectron spectroscopic study of the reaction of Li and Na with $NiCo_2O_4$, *Chem. Mater.*, 2005, **17**(20), 5202–5208.

17 Y. N. NuLi, P. Zhang, Z. P. Guo, *et al.*, $NiCo_2O_4$/C nanocomposite as a highly reversible anode material for lithium-ion batteries, *Electrochem. Solid-State Lett.*, 2008, **11**(5), A64–A67.

18 M. J. Aragón, B. León, C. Pérez Vicente, *et al.*, Cobalt oxalate nanoribbons as negative-electrode material for lithium-ion batteries, *Chem. Mater.*, 2009, **21**(9), 1834–1840.

19 G. Y. Hao, W. Wang, G. F. Gao, *et al.*, Preparation of nanostructured mesoporous $NiCo_2O_4$ and its electrocatalytic activities for water oxidation, *J. Energy Chem.*, 2015, **24**(3), 271–277.

20 S. M. Sun, S. D. Li, S. Wang, *et al.*, Fabrication of hollow $NiCo_2O_4$ nanoparticle/graphene composite for supercapacitor electrode, *Mater. Lett.*, 2016, **182**, 23–26.

21 T. Li, X. H. Li, Z. X. Wang, *et al.*, A novel $NiCo_2O_4$ anode morphology for lithium-ion batteries, *J. Mater. Chem. A*, 2015, **3**(22), 11970–11975.

22 S. J. Peng, L. L. Li, Y. X. Hu, *et al.*, Fabrication of spinel one-dimensional architectures by single-spinneret electrospinning for energy storage applications, *ACS Nano*, 2015, **9**(2), 1945–1954.

23 J. Liu, C. P. Liu, Y. L. Wan, *et al.*, Facile synthesis of $NiCo_2O_4$ nanorod arrays on Cu conductive substrates as superior anode materials for high-rate Li-ion batteries, *CrystEngComm*, 2013, **15**, 1578–1585.

24 Y. J. Chen, M. Zhuo, J. W. Deng, *et al.*, Reduced graphene oxide networks as an effective buffer matrix to improve the electrode performance of porous $NiCo_2O_4$ nanoplates for lithium-ion batteries, *J. Mater. Chem. A*, 2014, **2**, 4449–4456.

25 Y. Liu and Y. Chu, Surfactant-assisted synthesis of single crystal $BaWO_4$ octahedral microparticles, *Mater. Chem. Phys.*, 2005, **92**(1), 59–63.

26 M. P. Pileni, The role of soft colloidal templates in controlling the size and shape of inorganic nanocrystals, *Nat. Mater.*, 2003, **2**(3), 145–150.

27 S. Abouali, M. A. Garakani, Z. L. Xu, *et al.*, $NiCo_2O_4$/CNT nanocomposites as bi-functional electrodes for Li ion batteries and supercapacitors, *Carbon*, 2016, **102**, 262–272.

28 E. Umeshbabu, G. Rajeshkhanna and G. R. Rao, Urchin and sheaf-like $NiCo_2O_4$ nanostructures: Synthesis and electrochemical energy storage application, *Int. J. Hydrogen Energy*, 2014, **39**(28), 15627–15638.

29 C. T. Hsu and C. C. Hu, Synthesis and characterization of mesoporous spinel $NiCo_2O_4$ using surfactant-assembled dispersion for asymmetric supercapacitors, *J. Power Sources*, 2013, **242**(22), 662–671.

30 Y. D. Mo, Q. Ru, X. Song, *et al.*, 3-dimensional porous $NiCo_2O_4$ nanocomposite as a high-rate capacity anode for lithium-ion batteries, *Electrochim. Acta*, 2015, **176**, 575–585.

31 L. L. Li, Y. L. Cheah, Y. W. Ko, *et al.*, The facile synthesis of hierarchical porous flower-like $NiCo_2O_4$ with superior lithium storage properties, *J. Mater. Chem. A*, 2013, **1**(36), 10935–10941.

32 L. F. Shen, L. Yu, X. Y. Yu, *et al.*, Self-templated formation of uniform $NiCo_2O_4$ hollow spheres with complex interior structures for lithium-ion batteries and supercapacitors, *Angew. Chem., Int. Ed.*, 2015, **54**(6), 1868–1872.

33 Q. L. Wu, J. G. Xu, X. F. Yang, *et al.*, Ultrathin anatase TiO_2 nanosheets embedded with TiO_2-B nanodomains for lithium-ion storage: capacity enhancement by phase boundaries, *Adv. Energy Mater.*, 2015, **5**(7), 1401756–1401765.

34 T. Brezesinski, J. Wang, J. Polleux, *et al.*, Templated nanocrystal-based porous TiO_2 films for next-generation electrochemical capacitors, *J. Am. Chem. Soc.*, 2009, **131**(5), 1802–1809.